The Astrophysical Journal, 573:105–121, 2002 July 1

NOBEYAMA MILLIMETER ARRAY CO ($J = 1$–0) OBSERVATIONS OF THE Hα/RADIO LOBE GALAXY NGC 3079: GAS DYNAMICS IN A WEAK BAR POTENTIAL AND CENTRAL MASSIVE CORE

J. Koda,[1,2] Y. Sofue,[2] K. Kohno,[2] H. Nakanishi,[2] S. Onodera,[2] S. K. Okumura,[3] and Judith A. Irwin[4]

Received 2002 February 1; accepted 2002 March 7

ABSTRACT

We present ^{12}CO (1–0) observations in the central 4.5 kpc (1′) of the Hα/radio lobe galaxy NGC 3079 with the Nobeyama Millimeter Array. The molecular gas shows four components: a main disk, spiral arms, a nuclear disk, and a nuclear core. The main disk extends along the galaxy major axis. We detected its central 2 kpc radius, while its full extent is beyond our spatial coverage. Molecular gas is smoothly distributed in the main disk, having a gas mass of $5 \times 10^9\ M_\odot$ within the central $\sim$2 kpc radius. The spiral arms are superimposed on the main disk. Abrupt velocity changes of up to $\sim$200 km s^{-1} are observed along the spiral arms in S-shaped twists of isovelocity contours and double velocity-peaked features on the spectra. The nuclear disk with $\sim$600 pc radius appears in position-velocity (PV) diagrams, having an intense concentration of molecular gas. Its appearance on PV diagrams is indicative of oval motions of the gas, rather than circular. The nuclear disk and spiral arms form the so-called figure-of-eight pattern on a PV diagram. The nuclear core is more compact than our current resolution (2″ = 150 pc) and has a gas mass of $3 \times 10^8\ M_\odot$ within the central 150 pc. Although it is unresolved, the nuclear core shows a very high velocity $\sim$200 km s^{-1} even at the radius of $\sim$100 pc on the PV diagram. We propose a model that NGC 3079 contains a weak bar. The weak bar model explains the observed features of the main disk, spiral arms, and nuclear disk. The main disk and spiral arms result from gaseous x_1-orbits and associated crowding, respectively. The nuclear disk arises from gaseous x_2-orbits. The gas concentration in the nuclear disk could be explained by the expected gas-fueling mechanism: the gas on x_1-orbits flows along spiral arms (or offset shocks), colliding with the gas on x_2-orbits, and accumulating onto the nuclear disk. Assuming that the gas moves nearly along the spiral arms that run perpendicular to the line of sight, the pattern speed of the bar is estimated to be 55 ± 10 km s^{-1} kpc^{-1}. The high velocity of the nuclear core cannot be explained by our model for a bar. Thus we attribute it to a central massive core with a dynamical mass of $10^9\ M_\odot$ within the central 100 pc. This mass is 3 orders of magnitude more massive than that of a central black hole in this galaxy.

Subject headings: galaxies: active — galaxies: ISM — galaxies: kinematics and dynamics — galaxies: spiral — galaxies: structure

1. INTRODUCTION

NGC 3079 is a nearly edge-on ($i = 77°$) SBc galaxy at a distance of 15.6 Mpc (1″ corresponds to 76 pc; Sofue et al. 1999, see Table 1). Its nucleus is classified as a LINER (Heckman 1980) or Seyfert 2 galaxy (Ford et al. 1986; Ho, Fillipenko, & Sargent 1997; Sosa-Brito, Tacconi-Garman, & Lehnert 2001) from the optical emission spectrum and shows strong H_2O maser emission (Henkel et al. 1984; Nakai et al. 1995; Trotter et al. 1998). The overall velocity distribution of H_2O masers suggests the presence of a binding mass of $\sim 10^6\ M_\odot$ at the center (Trotter et al. 1998), possibly a central supermassive black hole, which has been found in many active galactic nuclei (AGNs) (Miyoshi et al. 1995; Wandel, Peterson, & Malkan 1999; Ishihara et al. 2001). Parsec-scale nuclear jets observed in the radio continuum may be outflow from the central compact object (Irwin & Seaquist 1988; Sawada-Satoh et al. 2000).

Kiloparsec-scale significant outflow along the galaxy minor axis is observed as lobes in the radio continuum (Duric & Seaquist 1988), Hα emission (Ford et al. 1986; Veilleux et al. 1994; Cecil et al. 2001; see Fig. 1), and X-ray emission (Fabbiano, Kim, & Trinchieri 1992; Pietcsh, Trinchieri, & Vogler 1998). Optical spectroscopy shows gas motions with a velocity range of $\sim$2000 km s^{-1} across the lobes and unusually high [N II]/Hα line ratios, which indicate the presence of shocks (Veilleux et al. 1994). This type of large-scale outflow is often attributed to starburst activity (Heckman, Armus, & Miley 1990). However, there are some arguments against this starburst model for NGC 3079 (Hawarden et al. 1995). Duric & Seaquist (1988) present an alternative model in which a wind flow from the nucleus could be directed toward the galaxy minor axis by interaction with dense gas surrounding the nucleus. This interaction produces shocks that explain the observed strength of H_2 emission from lower vibration transitions by collisional excitation (Hawarden et al. 1995).

At the root of the kiloparsec-scale outflow, there is a dense molecular disk with a radius of a few kiloparsecs (Young, Claussen, & Scoville 1988; Sofue & Irwin 1992; Irwin & Sofue 1992; Sofue et al. 2001). Based on their interferometry observations of CO ($J = 1$–0) emission, Sofue & Irwin (1992) found an intense concentration of gas in the molecular disk, spiral arm features visible on a position-velocity diagram, and a central compact core, which was unresolved at their resolution (4″). Recently, Sofue et al. (2001) have confirmed these features, and they further resolved and classified the innermost region into the nuclear

[1] JSPS Research Fellow; koda@ioa.s.u-tokyo.ac.jp.
[2] Institute of Astronomy, University of Tokyo, Mitaka, Tokyo 181-0015, Japan.
[3] Nobeyama Radio Observatory, Minamisaku, Nagano 384-1305, Japan.
[4] Department of Physics, Queen's University, Kingston, ON K7L 3N6, Canada.

TABLE 1
PROPERTIES OF NGC 3079

Parameter	Value	Reference
Morphology	SB(s)c sp	1
	Sc pec:	2
Nuclear activity	LINER	3
	Type 2 Seyfert	4
Position of nucleus:		5
α (B1950)	$9^{h}\,^{m}58\ 35\overset{s}{.}02$	
δ (B1950)	$55^{\circ}55'15\overset{''}{.}4$	
$D_{25} \times d_{25}$	7.9×1.4	1
B_T (mag)	11.54	1
P.A. (deg)	165	1
Inclination (deg)	77	6
Distance (Mpc)	15.6	5
Linear scale (pc arcsec^{-1})	76	
$S_{60\,\mu m}$ (Jy)	50.17 ± 0.054	7
$S_{100\,\mu m}$ (Jy)	103.40 ± 0.154	7
L_{FIR} ($L_{\odot}$)[a]	2.1×10^{10}	

REFERENCES.—(1) de Vaucouleurs et al. 1991; (2) Sandage & Tamman 1981; (3) Heckman 1980; (4) Ford et al. 1986; (5) Sofue & Irwin 1992; (6) Young et al. 1995; (7) Soifer et al. 1989.

[a] L_{FIR} was calculated as $3.75 \times 10^5 (D/\ \mathrm{Mpc})^2 (2.58 S_{60\,\mu m} + S_{100\,\mu m})$ in units of $L_{\odot}$.

molecular disk and ultra–high-density core, based on their appearance on intensity maps and position-velocity diagrams. (In this paper, we will reclassify the features based on our new data [§ 3] and on theoretical considerations [§ 4].) The molecular disk was also observed in HCN and HCO^+ (Kohno et al. 2001), which measure the concentration of high-density molecular clouds toward the nucleus.

The disk of NGC 3079 is rotating, with the north side approaching and south side receding. A K'-band image shows spiral arms in the disk, forming an inverted S-shaped pattern on the sky (Veilleux, Bland-Hawthorn, & Cecil 1999). If trailing spiral arms are assumed, the west of NGC 3079 is near-side, which is consistent with the entire dust lane morphology. NGC 3079 is a far-infrared (FIR) luminous galaxy listed in the *IRAS* bright galaxy catalog (Soifer et al. 1989). An *ISO* 90 μm map shows that most of the FIR emission is produced by dust heated by stars in the entire galaxy disk rather than the nucleus (Pérez García, Rodríguez Espinosa, & Fuensalida 2000). The H I disk extends more widely than the optical disk and shows warps at the outskirts (Irwin & Seaquist 1991). These warps may originate from an interaction with a nearby companion NGC 3073. The H I velocity field, however, shows a regular rotating-disk pattern. The radial emission profile is well fitted by an exponential function, while it shows a sharp drop in the central region ($<50''$; Irwin & Seaquist 1991), which is produced by absorption against strong continuum emission (Duric & Seaquist 1988). The CO disk is embedded in this region of the absorbed H I (Young et al. 1988; Sofue & Irwin 1992; Sofue et al. 1999) and coincident with a void of Hα line emission (Cecil et al. 2001).

Although NGC 3079 is classified as a barred galaxy (SBc), the stellar bar is hardly confirmed in optical/infrared photographs in this nearly edge-on galaxy. There is, however, some evidence for the presence of a bar. NGC 3079 has a stellar bulge that takes a so-called peanut shape (Shaw, Wilkinson, & Carter 1993), whose possible origin is a vertical instability of rotating disk-stars in a bar potential (Combes et al. 1990). Veilleux et al. (1999) fitted an oval orbit model to their Hα velocity field and concluded that

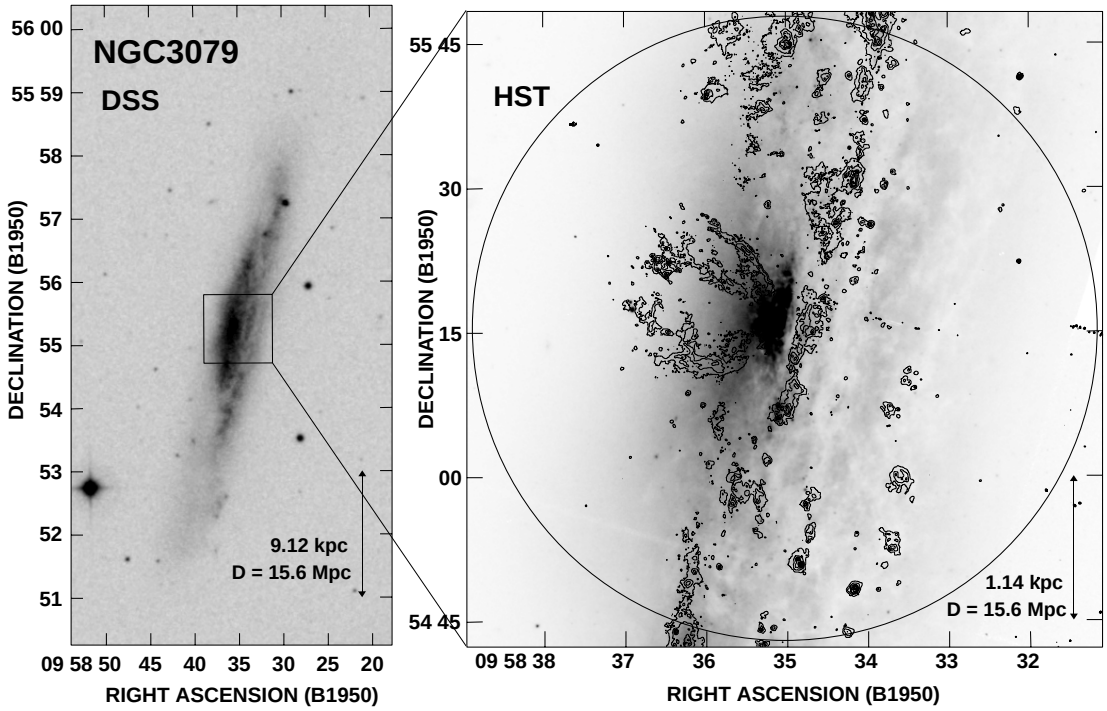

FIG. 1.—Optical images of NGC 3079. (*a*) *R*-band image from the Digitalized Sky Survey. (*b*) HST WFPC2 images of *I*-band (*gray scale*) and Hα+[N II] line emission (*contour*), obtained from the *HST* data archives (P.I. G. Cecil). Contours are at 2%, 5%, 15%, 20%, 30%, 40%, 50%, 60%, 70%, 80%, 90%, and 100% of the Hα+[N II] peak intensity. The circle represents the primary beam size of our CO (1–0) observations ($65''$ HPBW). The absolute positions of both panels were calibrated using the USNO-A2.0 catalog (Zacharias et al. 2000) and are uncertain to $0\overset{''}{.}5$.

bar streaming motions with moderately eccentric orbits ($e = b/a \sim 0.7$) aligned along P.A. $= 130°$ intrinsic to the disk (P.A. $= 163°$ on the sky[5]) are satisfactory to match the observations.

In this paper, we present our recent ^{12}CO ($J = 1$–0) observations of the central 1′ of NGC 3079 using the Nobeyama Millimeter Array (NMA). We describe the observations and data analysis in § 2. A part of the data has been published in Sofue et al. (2001), but this paper presents our new analyses including new observations. The main features in the molecular disk of NGC 3079 are presented in § 3. Gas dynamics in the molecular disk are discussed in § 4. A weak bar and central massive core explain all the observed features. The central rotation curve and mass are derived in § 5. We summarize our conclusions in § 6.

2. OBSERVATIONAL DATA

2.1. NMA ^{12}CO ($J = 1$–0) *Observations*

Our aperture synthesis observations of the ^{12}CO ($J = 1$–0) emission from NGC 3079 were obtained with the Nobeyama Millimeter Array (NMA) at the Nobeyama Radio Observatory (NRO),[6] between 2000 January and 2001 April for a single pointing center at (α1950, δ1950) $= (9^h58^m35^s.02, +55°55'15''.40)$. We made the observations with three available configurations (AB, C, and D); when combined, the visibility data cover projected baselines from 10 to 351 m. The NMA consists of six 10 m antennas, providing a FWHP of about 65″ at 115 GHz. The antenna size limits the minimum projected baseline, restricting the largest detectable size of objects to about 54″. Tunerless SIS receivers have receiver noise temperatures of about 30 K in double sideband and typical system noise temperatures of about 400 K in single sideband. Digital spectrocorrelators (Okumura et al. 2000) have two spectroscopic modes; we used a mode covering 512 MHz (1331 km s^{-1}) with 2 MHz (5.2 km s^{-1}) resolution. We observed the quasar 0954+556 every 20 minutes for gain calibration and 3C 279 (or 3C 273) for bandpass calibration. Absolute flux scales (0.68 Jy at 115 GHz for 0954+556, uncertain to ~20%) were measured three times in 2000 and once in 2001; no significant flux variation was observed.

The raw visibility data were calibrated for complex gain and passband with the UVPROC-II package, developed at NRO, and mapped with the NRAO/AIPS package. We applied the CLEAN procedure with natural weighting for each velocity channel and obtained a three-dimensional (R.A., decl., V_{LSR}) data cube. Parameters of the cube are listed in Table 2.

Figure 2 displays zeroth- and first-moment maps in the central 20″ × 48″ region (1.5 kpc × 3.7 kpc) of NGC 3079, while Figure 3 shows channel maps with an interval of 10.4 km s^{-1} in the same region. The significant emission (>3 σ; $1\sigma = 12$ mJy beam^{-1}) is detected in 63 adjacent channels within the velocity range of $V_{LSR} = 821$–1467 km s^{-1} ($\Delta V = 646$ km s^{-1}). No primary-beam correction has been applied in these maps. Figure 4 displays a position-velocity diagram (PV diagram) along the optically defined major axis (P.A. $= 165°$), integrated along the minor axis. The almost entire CO emission in Figure 2 (*left-hand panel*) falls in the slit-width (12″). The axes are labeled relative to the dynamical center and systemic recession velocity of the galaxy (derived in § 3.1.2; see Table 3).

Compared with single-dish observations from IRAM 30 m and FCRAO 14 m telescopes (Braine et al. 1993; Young et al. 1995), our NMA cube recovers about 87% of the total CO line flux in the central 23″ and 67% in 45″, which means that the CO emission is concentrated in the central region. We made no correction for the missing flux in the following discussion. Figure 5 compares a spectrum from our NMA cube with that from the IRAM observations (Braine et al. 1993). In order to obtain the fluxes and spectrum comparable to the single-dish ones, the NMA cube was corrected for the primary-beam response of antennas, convolved with the single-dish beam (23″ for IRAM and 45″ for FCRAO) and sampled at the pointing center of the single-dish observations.

TABLE 2
PARAMETERS OF CO (1–0) CUBE

Parameter	Value
Configuration	AB + C + D
Weighting	NA
Field of view (arcsec)	65
Synthesized beam:	
Major axis (arcsec)	1.9
Minor axis (arcsec)	1.6
P.A. (deg)	105
Velocity resolution (km s^{-1})	10.4
rms (mJy beam^{-1})	12

2.2. *Supplied HST Data*

We obtained images from the *Hubble Space Telescope* (*HST*) archive (P.I. G. Cecil; see Cecil et al. 2001). The images were taken with WFPC2 and two filters, F814W and F658N, which correspond to the *I*-band and Hα+[N II] filters in ground telescopes. The central part of NGC 3079 lies on a WFC chip rather than the PC chip. Cosmic-ray hits were removed and images are combined with the IRAF/STSDAS package. The absolute position of the *HST* images is calibrated using the USNO-A2.0 catalog (Zacharias et al. 2000) and is accurate to about 0″.5. The derived images are presented in the right-hand panel of Figure 1.

TABLE 3
KINEMATIC PARAMETERS OF THE MAIN DISK

Parameter	Value
Dynamical center:	
α (B1950)	$9^h58^m35^s.00$
δ (B1950)	$55°55'15''.90$
P.A (deg)	169
Inclination (deg)	79
V_{sys} (km s^{-1})	1147

[5] The bar position angle on the sky (P.A.$_{sky}$) is calculated from that intrinsic to the disk (P.A.$_{int}$) by $\tan(\text{P.A.}_{gal} - \text{P.A.}_{sky}) = \tan(\text{P.A.}_{gal} - \text{P.A.}_{int}) \cos i$, using their adopted position angle and inclination of the disk.

[6] Nobeyama Radio Observatory is a branch of the National Astronomical Observatory, operated by the Ministry of Education, Culture, Sports, Science and Technology, Japan.

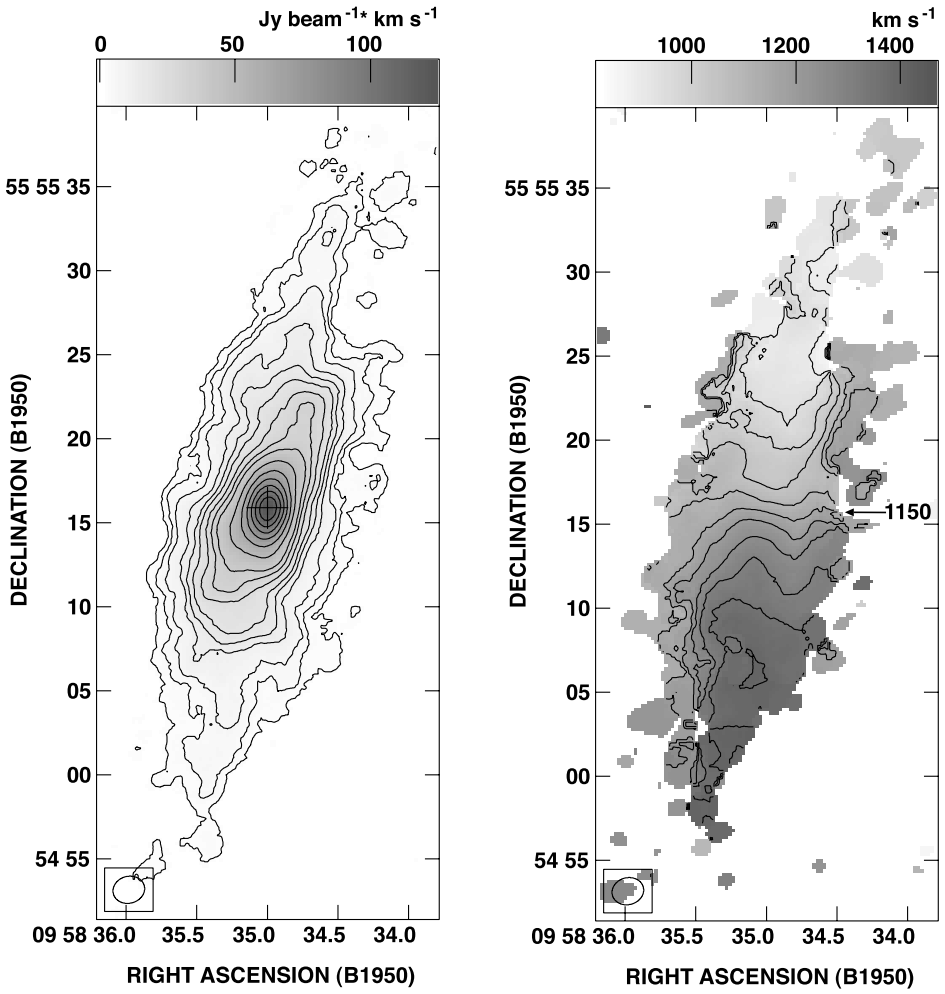

FIG. 2.—CO (1–0) zeroth- and first-moment maps in the central $20'' \times 48''$ (1.5 kpc × 3.7 kpc) region of NGC 3079. The synthesized beam ($1''.9 \times 1''.6$) is shown in the lower left-hand corners. *Left:* The zeroth-moment map (integrated-intensity map). Contour levels are 1.5%, 3%, 5%, 9%, 12%, 15%, 20%, 25%, 30%, 40%, 50%, 60%, 70%, 80%, 90%, and 100% of the peak integrated-intensity 1.25×10^2 Jy beam^{-1} km s^{-1}. The clip level was set to 2.5 σ, where 1 σ = 12 mJy beam^{-1}. The primary-beam attenuation has not been corrected. *Right:* The first-moment map (intensity-weighted mean-velocity map). Contours are drawn with an interval of 50 km s^{-1}. The contour of 1150 km s^{-1} (V_{sys} = 1147 km s^{-1}) is indicated by an arrow. The clip level was set to 4 σ to make this map.

3. RESULTS

Our maps and PV diagram show four distinct components: a main disk, spiral arms (or offset ridges), a nuclear disk, and a nuclear core. Figure 6 shows a schematic illustration of these four components on a PV diagram. We describe each of the four in order of decreasing radius in §§ 3.1–3.4 and compare them with previous results in § 3.5.

3.1. *The Main Disk*

3.1.1. *Smooth Gas Distribution on the Main Disk*

The zeroth-moment map of Figure 2 displays a disk with an extent of $45'' \times 15''$ (3.4 kpc × 1.1 kpc), elongated along the optically defined major axis of the galaxy (P.A. = 165°). Since our synthesis observations have an intrinsic maximum limit of detectable scale (54″), larger components detected in single-dish observations[7] are not covered in this map, and result in the missing flux (our total flux recovery is about 67% in 45″). The inclination of the galaxy (77°) is large, but it suffices to show the emission distribution on the disk, because the vertical sizes of molecular disks are usually thin (150 pc for the Galaxy from Clemens, Sanders, & Scoville 1988; 230 pc for NGC 891 from Handa et al. 1992) in comparison with the full extents of molecular disks (3.4 kpc or 45″ for NGC 3079 from the zeroth-moment map). The CO emission is smoothly distributed on the full disk, showing no emission-deficient regions often found in molecular disks (see Sakamoto et al. 1999a; Regan et al. 2001). The emission distribution is nearly axisymmetric, except for slight enhancements owing to spiral arms (see § 3.2). The main disk coincides with the void of H II regions (Cecil et al. 2001; see also the Fig. 7, *left-hand panel*), and with the region where the H I gas is observed in absorption (Irwin & Seaquist 1991) against strong radio continuum emission (Duric & Seaquist 1988). The center of the main disk coincides with the root of the Hα lobe.

3.1.2. *Kinematics of the Main Disk*

The first-moment map (Fig. 2, *right-hand panel*) shows a rotating disk with the north side approaching and south side receding. The S-shaped twists of isovelocity contours should

[7] Recently, NRO 45 m telescope observations found that the full extent of CO emission in NGC 3079 is about 80″ in radius (A. Yamauchi 2001, private communication).

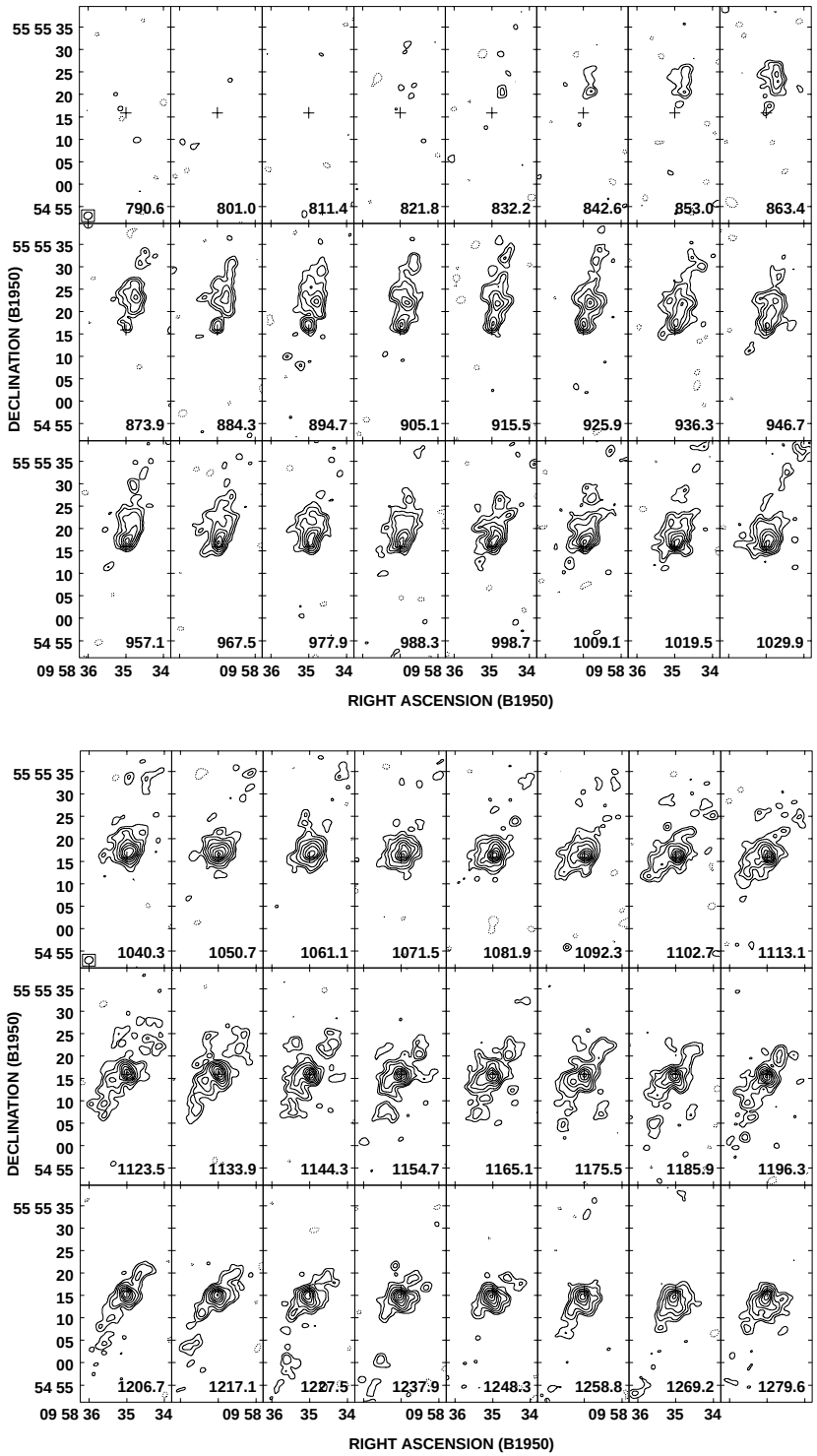

FIG. 3.—Channel maps in CO (1–0) emission. The channels have an interval of 10.4 km s^{-1}. Their central velocities (V_{LSR} in km s^{-1}) are labeled at the lower right-hand corners. Crosses show the position of the dynamical center (Table 3). Contour levels are -3, 3, 5, 8, 12, 16, 20, 25, and 30 σ, where 1 $\sigma = 12$ mJy beam^{-1}. Negative contours are dotted. No primary-beam correction has been applied.

be attributed to spiral arms (§ 3.2). The entire velocity field is almost perfectly bisymmetric, indicating regular motions in the molecular disk.

We obtained kinematical parameters from the first-moment map using the AIPS/GAL package. The dynamical center, position angle, and inclination are first determined using the Brandt rotation curve model (Brandt 1965). Then we fixed the above parameters, fitted tilted ring models with constant velocities to the first-moment map, and obtained the systemic recession velocity (LSR velocity). The results are listed in Table 3. The dynamical center coincides spatially with the emission-peak position: (α1950, δ1950) = ($09^h58^m35^s.00$, $+55^\circ55'15''.80$). The position angle and inclination are in good agreement with the results from optical isophotes (Sandage & Tamman 1981; Veilleux et al. 1999) and from kinematics of the H I gas (Irwin & Seaquist

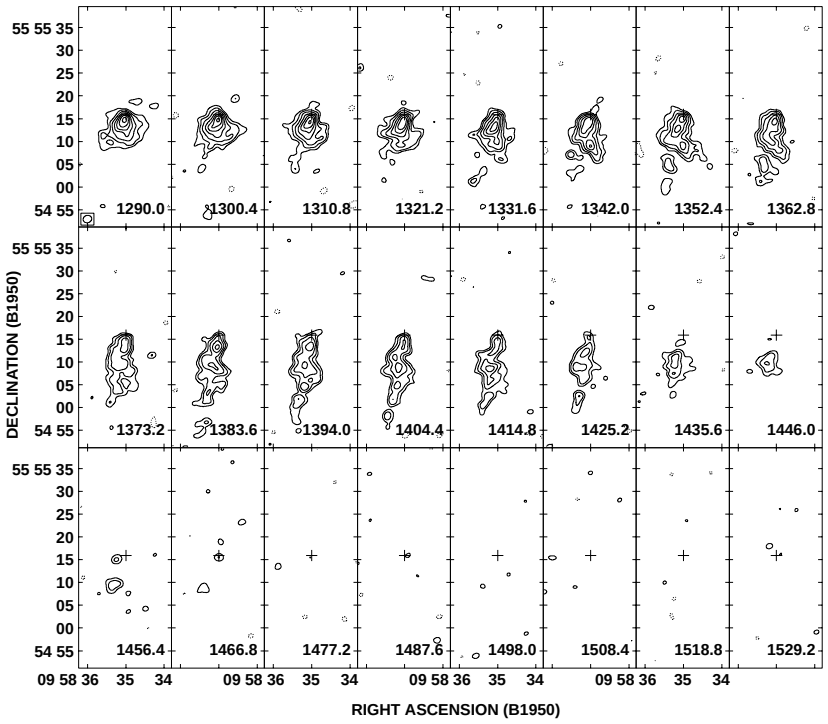

FIG. 3.—*Continued*

1991). The systemic recession velocity is consistent with estimates from optical spectroscopic data (e.g., 1150 km s^{-1}; Veilleux et al. 1999) but slightly exceeds the value from H I data (1124 km s^{-1}; Irwin & Seaquist 1991). This difference might come from a warp of the H I disk (Irwin & Seaquist 1991). We adopt the values from large-scale isophotes for position angle and inclination and the derived values for galaxy center and systemic recession velocity in the rest of our analysis. These choices do not affect the following discussion.

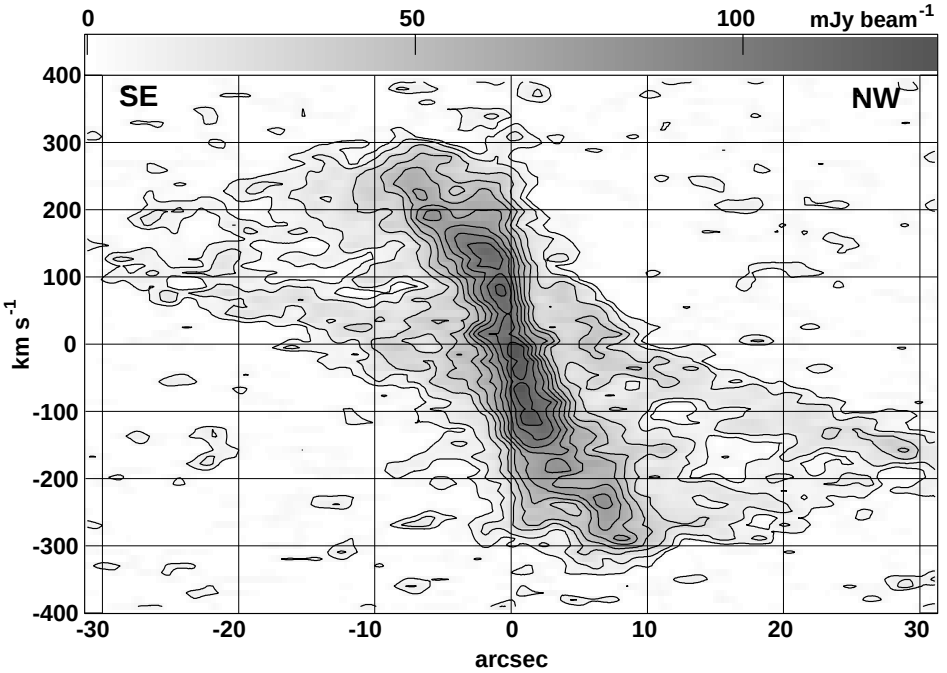

FIG. 4.—PV diagram of CO (1–0) emission along the major axis of NGC 3079 (P.A. = 165°). The slit width was set to be 12″, containing almost the entire emission in Fig. 2. The axes are labeled relative to the dynamical center and systemic recession velocity (Table 3). Velocities have been corrected for inclination (77°). Contours are at 5%, 10%, 20%, 30%, 40%, 50%, 60%, 70%, 80%, 90%, and 100% of the peak intensity.

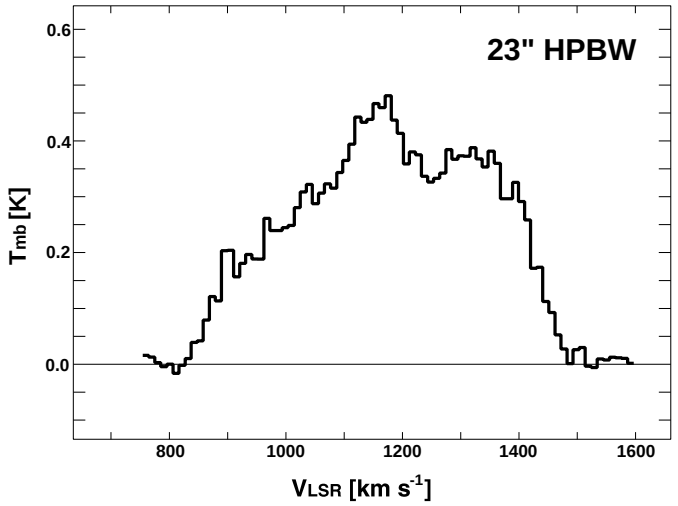

FIG. 5.—Comparison of our CO (1–0) line spectrum with the single-dish result of IRAM 30 m from Braine et al. (1993). The NMA cube was corrected for primary-beam attenuation, convolved with the single-dish beam size (23″) of IRAM, and sampled at the pointing centers of the IRAM observations (α1950, δ1950) = ($09^h58^m35^s.4$, $+55°55'11''.0$). The gray line show the spectrum from the IRAM observations, whereas the black line show that from the NMA cube.

The PV diagram (Fig. 4) shows the main disk as two ridges, symmetrically extending southeast and northwest from the velocity peaks around the center (see also Fig. 6). The near-perfect symmetry in the diagram again indicates regular motions of the molecular gas in the disk. The velocity of 220 km s^{-1} at the radius of 26″ (2.0 kpc) indicates the dynamical mass of $M_{\rm dyn} = 2.2 \times 10^{10}\ M_\odot$. The disk is also confirmed in the channel maps (Fig. 3); the approaching (northwest) side appears in the channels of $V_{\rm LSR}$ = 821–1029 km s^{-1}, while the receding (southeast) side is found in $V_{\rm LSR}$ = 1258–1467 km s^{-1}.

3.1.3. *Mass and Surface Densities of the Molecular Gas*

Masses of molecular gas $M_{\rm H_2}$ are estimated from total CO-line flux $S_{\rm CO}$, CO-to-H_2 conversion factor $X_{\rm CO}$, and galaxy distance D by

$$\left(\frac{M_{\rm H_2}}{M_\odot}\right) = 7.2 \times 10^3 \left(\frac{D}{\rm Mpc}\right)^2 \left(\frac{S_{\rm CO}}{\rm Jy\ km\ s^{-1}}\right) \times \left[\frac{X_{\rm CO}}{1.8 \times 10^{20}\ \rm cm^{-2}\ (K\ km\ s^{-1})^{-1}}\right]. \quad (1)$$

Assuming the hydrogen mass fraction (0.707 from Cox et al. 2000), the total gas mass, including He and other elements, becomes $M_{\rm gas} = 1.41 M_{\rm H_2}$. Face-on surface densities of molecular gas are calculated from the integrated CO line intensity $I_{\rm CO}\Delta V$, galaxy inclination i, and conversion factor $X_{\rm CO}$ by

$$\left(\frac{\Sigma_{\rm H_2}}{M_\odot\ \rm pc^{-2}}\right) = 3.0 \times 10^2 \cos i \left(\frac{I_{\rm CO}\Delta V}{\rm Jy\ km\ s^{-1}\ arcsec^{-2}}\right) \times \left[\frac{X_{\rm CO}}{1.8 \times 10^{20}\ \rm cm^{-2}\ (K\ km\ s^{-1})^{-1}}\right]. \quad (2)$$

The surface density of total gas also becomes $\Sigma_{\rm gas} = 1.41\Sigma_{\rm H_2}$. The surface density estimation is independent of galaxy distance. We adopt the conversion factor of $X_{\rm CO} = 1.8 \times 10^{20}$ cm^{-2} (K km s^{-1})$^{-1}$ from observations in the Galaxy (Dame, Hartmann, & Thaddeus 2001), while $X_{\rm CO}$ could be smaller in galactic center regions (Arimoto, Sofue, & Tsujimoto 1996).

The total flux within the radius of 26″ is $S_{\rm CO} = 1.9 \times 10^3$ Jy km s^{-1}, which corresponds to $M_{\rm gas} = 4.6 \times 10^9\ M_\odot$ for the galaxy distance $D = 15.6$ Mpc. The ratio of dynamical mass ($2.2 \times 10^{10}\ M_\odot$ from § 3.1.2) to the total molecular gas mass $M_{\rm gas}/M_{\rm dyn}$ is about 21% within the radius of 2 kpc. The peak integrated intensity is $I_{\rm CO}\Delta V = 1.3 \times 10^2$ Jy beam^{-1} km s^{-1} (or 3.8×10^3 K km s^{-1}) at (α1950, δ1950) = ($09^h58^m35^s.00$, $+55°55'15''.80$); the corresponding face-on surface density becomes $\Sigma_{\rm gas} = 2.5 \times 10^3\ M_\odot$ pc^{-2}. No correction for missing flux is applied.

Figure 8 shows the radial profile of the CO emission. Integrated intensities are azimuthally averaged in each annulus ($\Delta r = 0''.5$) with corrections for inclination (77°) and primary-beam attenuation. The outskirts of the profile ($r > 5''$) is well fitted by an exponential (*dotted line*). At the innermost region, the CO emission exceeds this exponential curve, indicating a high CO concentration at the central region. Surface densities of molecular gas are labeled at the right-hand axis. The observed value of $\Sigma_{\rm H_2}$ = 1000 $M_\odot$ pc^{-2} at $r \sim 5''$ (380 pc) is an order of magnitude higher than the typical value for the central regions of nearby galaxies (Sakamoto et al. 1999b).

The H I gas surface density also follows an exponential profile $\Sigma^0_{\rm H\,I}\, e^{-r/h_{\rm H\,I}}$, where $h_{\rm H\,I} = 118''$ (9.0 kpc) and $\Sigma^0_{\rm H\,I} = 8.8 \times 10\ M_\odot$ pc^{-2} (Irwin & Seaquist 1991, from their Table 4). In comparison with this H I profile, our H_2 profile (*dotted line*) takes the same surface density at nearly the edge of our detected molecular disk ($r \sim 23''$ or 1.7 kpc), rising more steeply toward the galaxy center ($h_{\rm CO} \sim 7''.2$ or 550 pc). This indicates that the gas in NGC 3079 is highly concentrated in the central molecular disk.

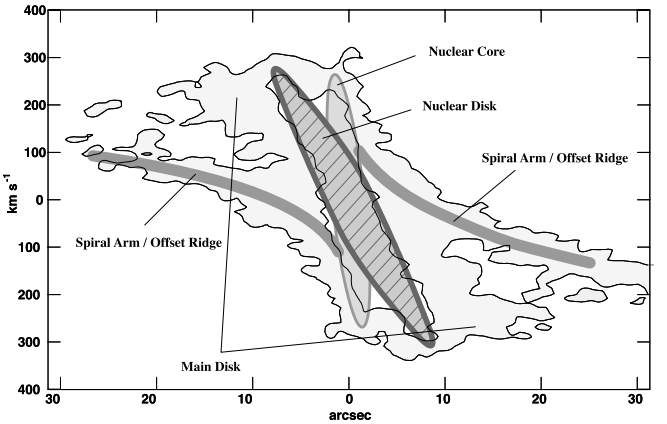

FIG. 6.—Schematic illustration of PV diagram. Four distinct components exist in the molecular disk of NGC 3079: main disk, spiral arms (or offset ridges), nuclear disk, and nuclear core.

3.2. *The Spiral Arms/Offset Ridges*

The zeroth-moment map (Fig. 2, *left-hand panel*) shows armlike enhancements of emission superimposed on the

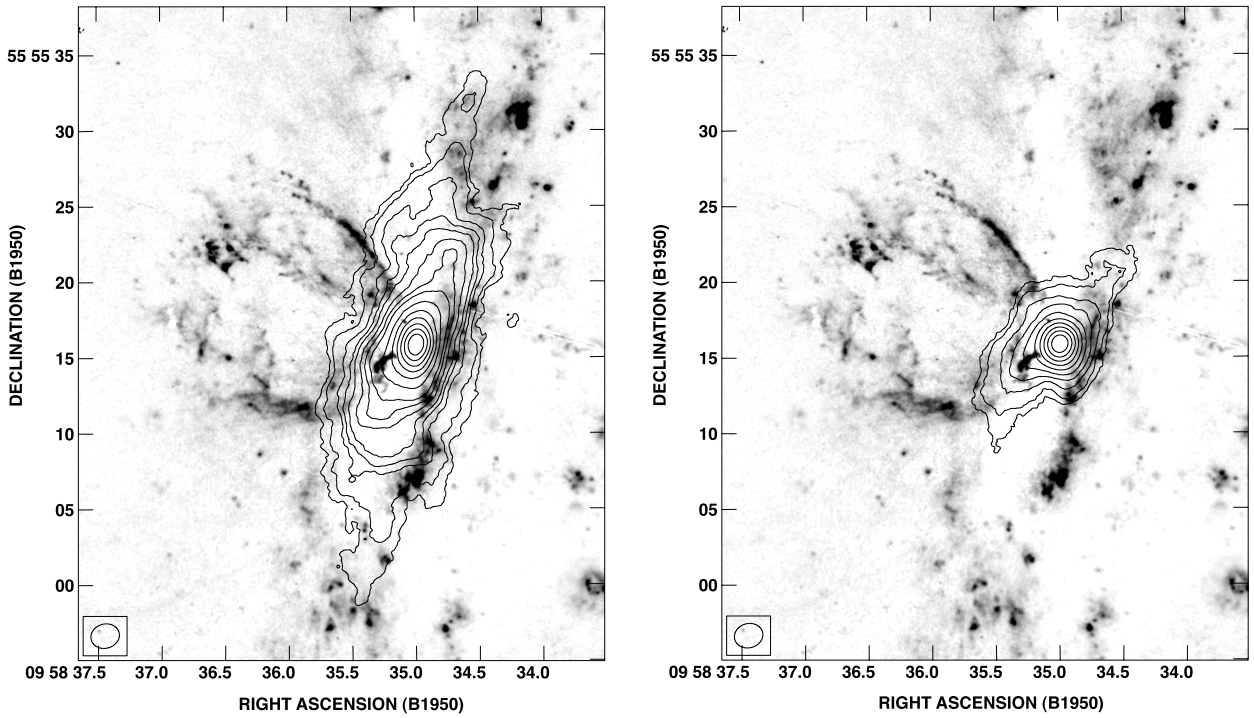

FIG. 7.—Comparisons of CO maps (*contours*) with the Hα+[N II] map (*gray scale*; from the *HST* archives). The absolute position of the *HST* image was calibrated with the USNO-A2.0 catalog and is accurate to about 0.″5. The ellipses at the lower left-hand corners show the synthesized beam for the CO observations. The two panels show two sets of CO zeroth-moment maps with different integrated velocity ranges. *Left:* The CO map (*contours*) is derived by integrating the cube in the full velocity range where CO emission is detected. Contour levels are 3%, 5%, 9%, 12%, 15%, 20%, 25%, 30%, 40%, 50%, 60%, 70%, 80%, 90%, and 100% of the peak integrated intensity 1.25×10^2 Jy beam^{-1} km s^{-1}. The molecular disk coincides with the void of H II regions at the center, and its center is coincident with the root of the Hα lobe. *Right:* The CO map (*contours*) is derived by integrating the cube in the velocity range where the spiral arms are dominant in emission ($\Delta V = \pm 100$ km s^{-1}). Contour levels are 5%, 10%, 20%, 30%, 40%, 50%, 60%, 70%, 80%, 90%, and 100% of the peak integrated intensity 6.52×10 Jy beam^{-1} km s^{-1}. The spiral arms extend from the root of the Hα lobe and form a S-shaped pattern.

main disk; two ridges bisymmetrically run northwest and southeast from the galaxy center (most obvious within the central $\sim$10″ radius), forming an *inverted* S-shaped pattern. These features resemble (trailing) spiral arms or offset ridges, which are often found at the leading edge of stellar bars. (Note that although these enhancements in the zeroth-moment map do arise from the spiral arms, they are slightly offset from the actual spiral arms [see Fig. 7], because this projected map is contaminated by emission from other components.) The S-shaped twists of isovelocity contours on the first-moment map (Fig. 2, *left-hand panel*) coincide with the two arms, indicating noncircular motions around the spiral arms. Similar inverted S-shaped spiral arms have been found in a K'-band image (Veilleux et al. 1999).

Figure 9 shows line profiles of CO emission at 5×7 points on a 3″ spacing grid (*crosses in the left-hand panel*), centered at the dynamical center (Table 3). Remarkable double-peaked features appear along the spiral arms:

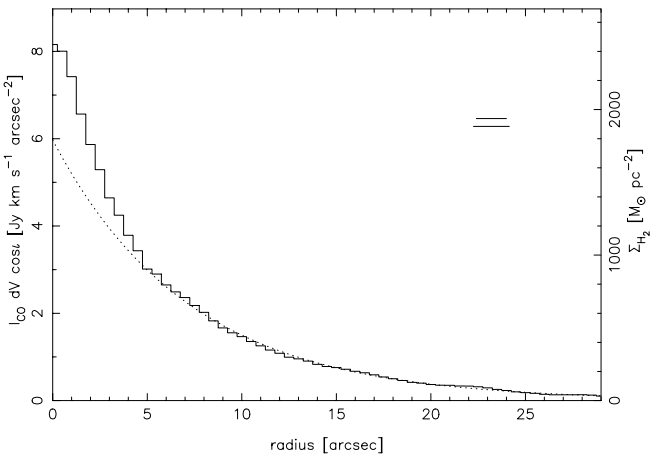

FIG. 8.—Radial distribution of CO emission. CO integrated intensities are azimuthally averaged with corrections for inclination and primary-beam attenuation. No correction for missing flux (about 10%–30%) has been applied. The surface densities on the right-hand axis are calculated by assuming the Galactic conversion factor $X_{CO} = 1.8 \times 10^{20}$ cm^{-2} (K km s^{-1})$^{-1}$ (Dame et al. 2001). The two horizontal bars show the beam size along the major and minor axes (1.″9 × 1.″6). The solid line presents the derived emission profile, while the dotted line shows a fitted exponential profile, i.e., $5.97 \exp(-r/7.''24)$, at radii of $r > 5''$.

TABLE 4

GAS AND DYNAMICAL MASSES

RADIUS[a]		M_{dyn}	M_{gas}[b]	M_{gas}/M_{dyn}
(arcsec)	(pc)	($10^9 M_\odot$)	($10^8 M_\odot$)	(%)
26.....	2.0×10^3	22	46 (26)	21 (12)
2.....	1.5×10^2	1.7	3.0 (1.7)	18 (10)
1.....	76	0.7	...	...

[a] Radius in the galactic plane.

[b] Gas mass is calculated with a conversion factor $X_{CO} = 1.8 \times 10^{20}$ cm^{-2} (K km s^{-1})$^{-1}$ and the H abundance $X = 0.707$. The values in brackets are the ones with $X_{CO} = 1.0 \times 10^{20}$ cm^{-2} (K km s^{-1})$^{-1}$ for high-metallicity regions such as galactic centers (Arimoto et al. 1996).

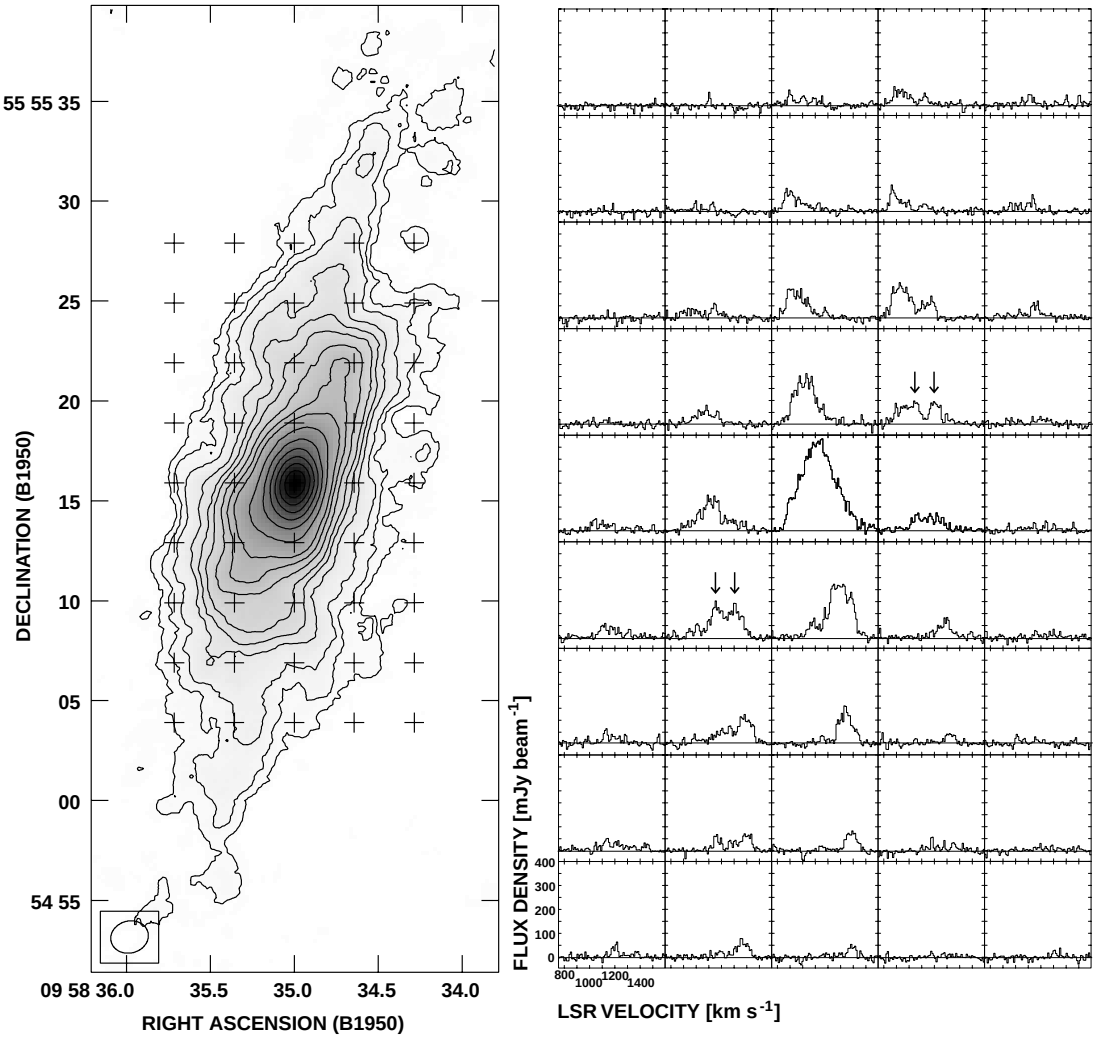

FIG. 9.—CO (1–0) line profiles and zeroth-moment map for reference. The line profiles are sampled at 5×7 points on the $3''$ spacing grid (*crosses in the left-hand panel*), centered at the dynamical center (Table 3). Double-peaked features in the line profiles are observed along the spiral arms: arrows point to two examples. The double peaks originate from distinct velocities between the main disk and spiral arms (or offset ridges).

arrows point to examples of the double peaks. The northwest arm corresponds to peaks with higher velocities, while the southeast arm corresponds to peaks with lower velocities. The other peaks come from the main disk. These distinct velocities between the main disk and spiral arms (typically $\Delta V \sim 200$ km s^{-1}) produce the S-shaped twists in the first-moment map. Similar double-peaked features have been noticed from Hα-spectroscopic data (Filippenko & Sargent 1992; Veilleux et al. 1999), although their low velocity resolution did not allow them to distinguish between the main disk and spiral arms.

The spiral arms are also confirmed on the PV diagram (Fig. 4; see also Fig. 6). Two ridges run northwest and southeast with lower velocities than those of the main disk. These two ridges and a central ridge of the nuclear disk (§ 3.3) show a so-called figure-of-eight pattern (or "tilted X" pattern). Similar patterns are often found in edge-on barred galaxies (Handa et al. 1990; García-Burillo & Guélin 1995; Laine et al. 1999; Merrifield & Kuijken 1999). In the velocity range of $\Delta V = \pm 150$ km s^{-1} ($V_{\rm sys} = 1147$ km s^{-1}), the spiral arms are more dominant in emission than the main disk.

This is also evident in the channel maps (Fig. 3). The spiral arms are confirmed at $V = 1010$–1280 km s^{-1}; emission from the northwest and southeast arms appear at the northwest and southeast edges of maps at 1010 and 1280 km s^{-1}, approaching the innermost core with increasing and decreasing velocities, respectively. Figure 7 (*right-hand panel*) shows contours of a zeroth-moment map made in the velocity range of $\Delta V = \pm 100$ km s^{-1} centered at the systemic recession velocity (superimposed on the Hα+[N II] map). The spiral arms are rooted to the nucleus, forming an inverted S-shaped pattern on the sky.

3.3. *The Nuclear Disk*

The nuclear disk shows a sign of an existence on the PV diagram (Fig. 4): remarkable velocity peaks appear symmetrically at ($-7''$, $+250$ km s^{-1}) and ($+7''$, -250 km s^{-1}). Figure 10 shows PV diagrams with $1''$ width and offsets of $+2''$, $0''$, and $-2''$ along the galaxy minor axis. The cuts are along the galaxy major axis. These diagrams reveal that the two peaks are on a single kinematical sequence: ridges are running and connecting the two peaks through three panels

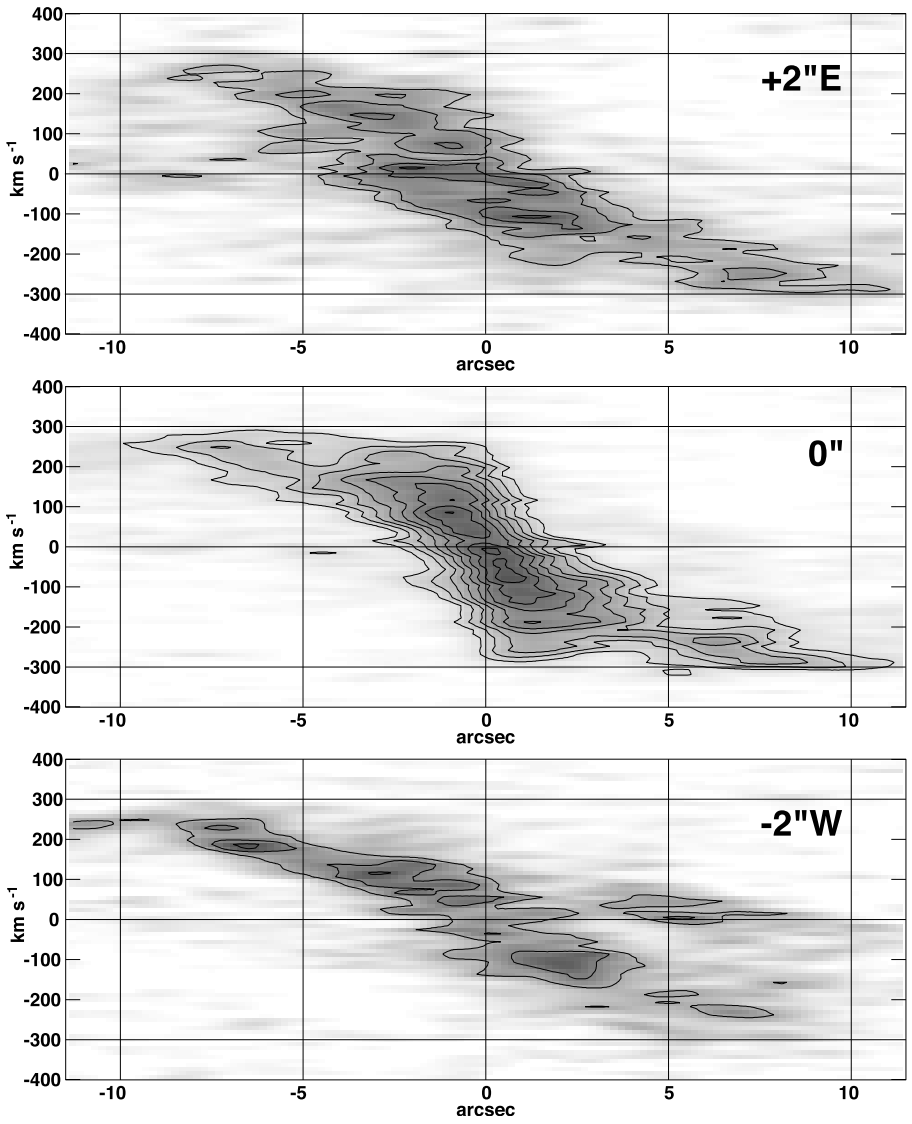

FIG. 10.—PV diagrams along the major axis (P.A. = 165°) with offsets along the minor axis of +2″, 0″, and −2″ (*the plus sign denotes east*). The slit widths are 1″. The axes are labeled relative to the dynamical center and systemic recession velocity (Table 3). Velocities have been corrected for inclination (77°). Contours in all the panels are at 2, 3, 4, 5, 6, 7, 8, 9, and 10 times 4.0×10^{-2} Jy beam^{-1}.

(see also Fig. 6). This sequence seems to be rotating in this innermost region and forming a nuclear disk. The nuclear disk is obviously distinct from other velocity peaks in the innermost region (at ±1″ in Fig. 4), because their corresponding peaks appear only in the diagram with 0″ offset; we thus think that they are consequences of the nuclear core (see § 3.4). The very high CO concentration within the nuclear disk ($r < 7''$; Figs. 4 and 8) indicates its distinct nature from the main disk. We conclude that the component which appears as the peaks and ridges in the PV diagrams is the nuclear disk. This component is rotating around the galaxy center with the north side approaching and south side receding.

In the three panels of Figure 10, the ridges corresponding to the nuclear disk are not on a straight line connecting their two velocity peaks: the ridges are bent downward and upward in the +2″ and −2″ offset diagrams, respectively, while the ridge twists upward (*left-hand side*) and downward (*right-hand side*) in the 0″ offset diagram. The deviations from the straight line amount to ∼50 km s^{-1}. These symmetrical bends and twist indicate that the gas in the nuclear disk takes oval orbits rather than circular (see § 4).

The nuclear disk is also seen in the channel maps (Fig. 3). The two velocity peaks on the PV diagrams appear in the channels of $V_{\rm LSR} = 822$–926 km s^{-1} as an emission peak at around 7″ north from the center and in $V_{\rm LSR} = 1384$–1467 km s^{-1} at around 7″ south. In other channels, strong emission from the main disk and nuclear core contaminates the nuclear disk emission.

3.4. *The Nuclear Core*

The nuclear core is most clearly seen in the PV diagram (Fig. 4), which appears as two velocity peaks at (−1″, +240 km s^{-1}) and (+1″, −240 km s^{-1}). The distinct kinematics of this core from the other components is evident in a series of PV diagrams which have positional offsets along the galaxy minor axis (Fig. 10). Among the three diagrams with +2″, 0″, and −2″ offsets, the nuclear core appears only in the central one. The high velocities indicate a large dynamical mass

in this nuclear region if the gas is pure-circularly rotating; we will discuss this in § 4.4.

The zeroth-moment map (Fig. 2) shows the nuclear core as an intense CO concentration at the very center of the galaxy. It is also confirmed in channel maps (Fig. 3) in almost all the velocities ($V_{\rm LSR} = 863$–1436 km s^{-1}). The central gas density of the nuclear core is as high as $2.5 \times 10^3\ M_\odot$ pc^{-2}, which is about an order of magnitude higher than is typical for nearby normal galaxies (Sakamoto et al. 1999a). This value is, however, a lower limit, because the core is unresolved even in our high-resolution observations ($1\farcs9 \times 1\farcs6$), The total flux within the radius of $2''$ (152 pc) is $S_{\rm CO} = 1.2 \times 10^2$ Jy km s^{-1}; the corresponding gas mass is $M_{\rm gas} = 3.0 \times 10^8\ M_\odot$.

3.5. *Comparison with Previous Results*

On the molecular disk of NGC 3079, Sofue & Irwin (1992) identified three main components: an outer disk, spiral arms, and a central compact core. Recently, Sofue et al. (2001) further resolved the central compact core and classified it into two distinct components, a nuclear molecular disk and an ultra–high-density molecular core, based on their appearance on maps and PV diagrams. In this paper, we reclassified the observed features into four distinct components, based on our new observations and analyses and partly on theoretical considerations in § 4. The outer disk and spiral arms in Sofue & Irwin (1992) correspond to our main disk and spiral arms, respectively, and the ultra–high-density molecular core in Sofue et al. (2001) corresponds to our nuclear core. The nuclear molecular disk in Sofue et al. (2001) is different from our nuclear disk and includes both our nuclear disk and main disk in part.

We confirmed two peaks on a PV diagram in the central region, reported by Sofue & Irwin (1992), in Figure 10. This feature, however, cannot be confidently attributed to the nuclear ring (Sofue & Irwin 1992) because the two peaks may arise from our nuclear disk (see Fig. 10, *top* and *bottom panels*) superposed on our nuclear core. Our central surface density, $\Sigma_{\rm gas} = 2.5 \times 10^3\ M_\odot$ pc^{-2}, is consistent with the value ($2.2 \times 10^4\ M_\odot$ pc^{-2}) of Sofue & Irwin (1992) by considering the difference of the adopted conversion factors and applying the correction for inclination to the value of Sofue & Irwin (1992). We could not find unambiguous evidence for molecular outflow (Irwin & Sofue 1992) in our data.

4. GAS DYNAMICS IN NGC 3079

The near-perfect bisymmetric structures of the molecular disk are striking. These kinds of bisymmetry are often thought to be consequences of gas motions in a bar. Although a stellar bar is not seen in optical/infrared photographs in this nearly edge-on galaxy, there is some indirect evidence for the presence of a bar: the peanut-shaped bulge (Combes et al. 1990; Shaw, Wilkinson, & Carter 1993); the figure-of-eight pattern on the PV diagram (Kuijken & Merrifield 1995); the high central concentration of the molecular gas (Sakamoto et al. 1999b); and the fact that the Hα velocity field is well fitted by an oval-orbit model in a weak bar (Veilleux et al. 1999). We thus propose a model that NGC 3079 contains a weak bar. This model naturally explains the features in § 3: the main disk and spiral arms (or offset ridges) may result from gaseous x_1-orbits and associated crowding, respectively. The nuclear disk may arise from gaseous x_2-orbits. This model, however, cannot interpret the nuclear core, which necessitates a massive component besides the bar at the galaxy center. Figure 11 shows schematic views of our interpretation, drawn on our model orbits (see a description in § 4.1). We present below our detailed case for the existence of the weak bar and discuss the origin of the main disk, spiral arms, nuclear disk, and core.

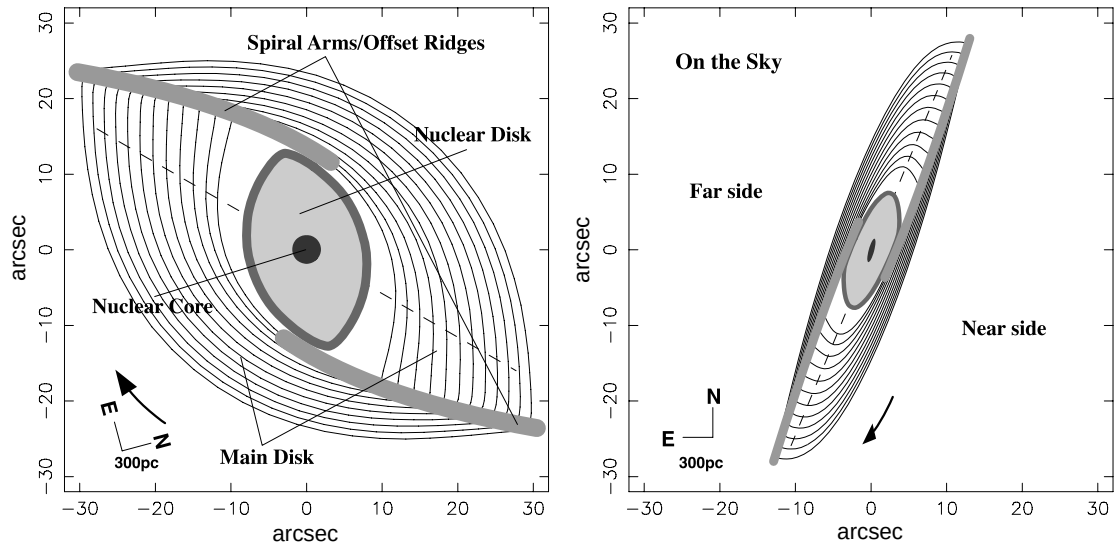

FIG. 11.—Schematic views of our interpretation of the molecular disk in NGC 3079. Four distinct components, the main disk, spiral arms/offset ridges, nuclear disk, and nuclear core, are drawn on the streamlines of our model orbits in the bar reference frame (§ 4.1). The bar has the position angle of 135° intrinsic to the galaxy from the north. *Left:* Face-on view. The galaxy major axis lies horizontally, while the bar runs along dashed line which is inclined clockwise by 30° from the horizontal. *Right:* Projection on the sky for P.A. = 165° and $i = 77°$.

4.1. *Damped-Orbit Model*

We adopt a damped-orbit model by Wada (1994) and Sakamoto, Barker, & Scoville (2000) to describe gas motions in a weak bar potential. This model solves an equation of motion that includes a damping-force term to emulate the collisional nature of the gas, and it obtains closed orbits for gas in a bar. This model has been applied to galaxy NGC 5005 (Sakamoto et al. 2000), and similar models have been successfully used to infer the presence of bars in edge-on galaxies that show characteristic patterns on PV diagrams (Binney et al. 1991; Achtermann & Lacy 1995; García-Burillo & Guélin 1995; Kuijken & Merrifield 1995).

Figure 12 displays our model of gas orbits in a bar potential that reproduces the main features in the zeroth- and first-moment maps and the PV diagram of NGC 3079. We here took the same potential model as Sakamoto et al. (2000) of

$$\Phi(r,\theta) = (1-\epsilon\cos 2\theta)\frac{v_0^2}{2}\log\left[1+(r/a)^2\right], \qquad (3)$$

where the first and second terms stand for disk and bar potentials, respectively, and θ is the azimuthal angle from the bar major axis. For this particular case we adopted the characteristic radius $a = 6''$ (456 pc), rotation velocity $v_0 = 240$ km s^{-1}, and bar strength $\epsilon = 0.04$ to match the observations. We chose the pattern speed of $\Omega_b = 55$ km s^{-1} kpc^{-1} based on consideration given in § 4.2. The inner and outer inner Lindblad resonances (ILRs) and corotation occur at the radii of 7.″7 (582 pc), 10.″5 (798 pc), and 57.″1 (4.34 kpc), respectively. We assumed that the position angle of the bar (*dashed line*) from the north is P.A.$_{\rm int} = 135°$ intrinsic to the disk and P.A.$_{\rm sky} = 158°$ on the sky. On the galaxy disk, this position angle of the bar differs by 30° from that of the galaxy major axis, which runs horizontally in Figure 12 (*top*).

Our parameters of the bar chosen to match the CO observations are in good agreement with the values that Veilleux et al. (1999) have derived by fitting an oval-orbit model to their Hα velocity field of NGC 3079 ($\Omega_b \sim 60$ km s^{-1} kpc^{-1}; P.A.$_{\rm bar} = 130 \pm 10°$; axes ratio of oval orbits 0.7). Beyond our particular choices of the parameters, the features of gaseous closed orbits described below are general (Wada 1994; Lindblad & Lindblad 1994) and have been established in numerical simulations (Wada 1994; Wada & Koda 2001; Koda & Wada 2002).

Closed orbits in a bar have an elongation in general; the position angle of the elongation ψ is measured clockwise from the bar major axis (top panel of Fig. 12, *dashed line*), in the rest of the discussion. For collisionless starlike particles, two families of closed orbits are dominant: x_1-orbits have an elongation with $\psi = 0°$ and dominate outside of the outer ILR and inside of the inner ILR, while x_2-orbits elongate with $\psi = 90°$ and are dominant between the ILRs. Orbits for gaseous particles show similar families at the same loci (Fig. 12, *top*), while gaseous x_1-orbits have an elongation toward the leading edge of the bar ($\psi > 0°$), and gaseous x_2-orbits elongate opposite ($\psi < 90°$), owing to the damping force.

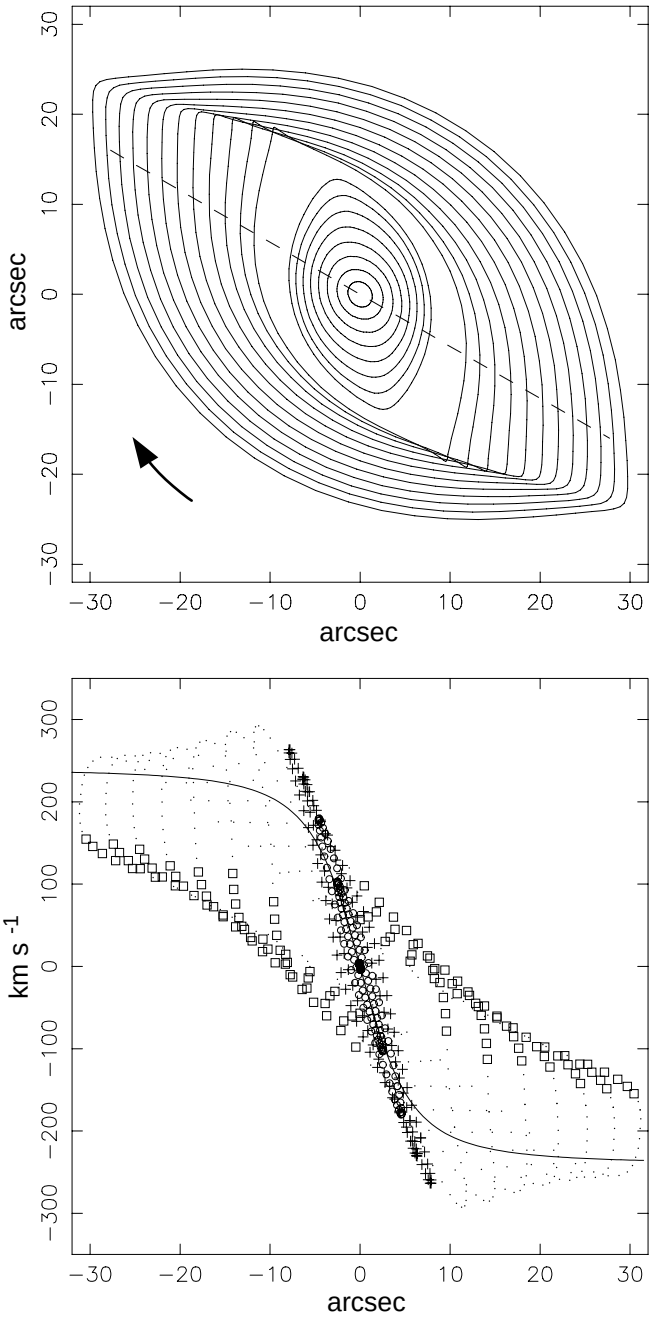

FIG. 12.—Model gas motions in the molecular disk of NGC 3079. *Top:* Face-on view of model orbits in a weak bar potential, on the frame rotating with the bar. The galaxy major axis runs horizontally. The bar is rotating clockwise, and runs along the dashed line (inclined from the horizontal by 30°). The orbits are calculated using a damped-orbit model (Wada 1994). The inner and outer ILR and corotation occur at the radii of 8″, 11″, and 57″ (1″ = 76 pc), respectively. *Bottom:* Model PV diagram, which cuts the model galaxy along the galaxy major axis, with the width containing the full region at the top panel. The solid line shows the circular rotation curve. Different symbols are used for different orbits: circles are x_1-orbits inside the inner ILR, crosses are x_2-orbits, squares are x_1-orbits outside the outer ILR on the downstream side of the sharp turns on the streamlines, and dots are also the x_1-orbits at the rests.

4.2. *The Origin of the Main Disk and Spiral Arms*

The main disk and spiral arms may originate from gaseous x_1-orbits. The position angle ψ of orbits changes with radius owing to the damping force, producing crowded regions of the orbits (Fig. 12). The crowding of the gaseous x_1-orbits that appear at the leading edge of the bar result in spiral arms (or so-called offset ridges), which are similar to those on the molecular disk of NGC 3079. The slightly

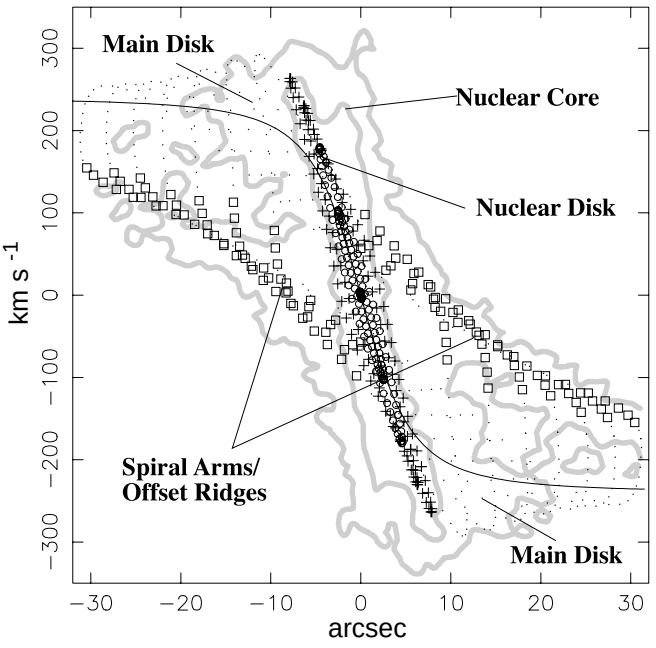

FIG. 13.—Comparison of the model and observed PV diagrams. Contours trace the observed PV diagram (Fig. 4) at 8% and 40% of the peak intensity. Symbols plotted are the same as those in the bottom panel of Fig. 12. Our model reproduces the main features of the molecular disk of NGC 3079 except the nuclear core. This indicates the presence of a massive core.

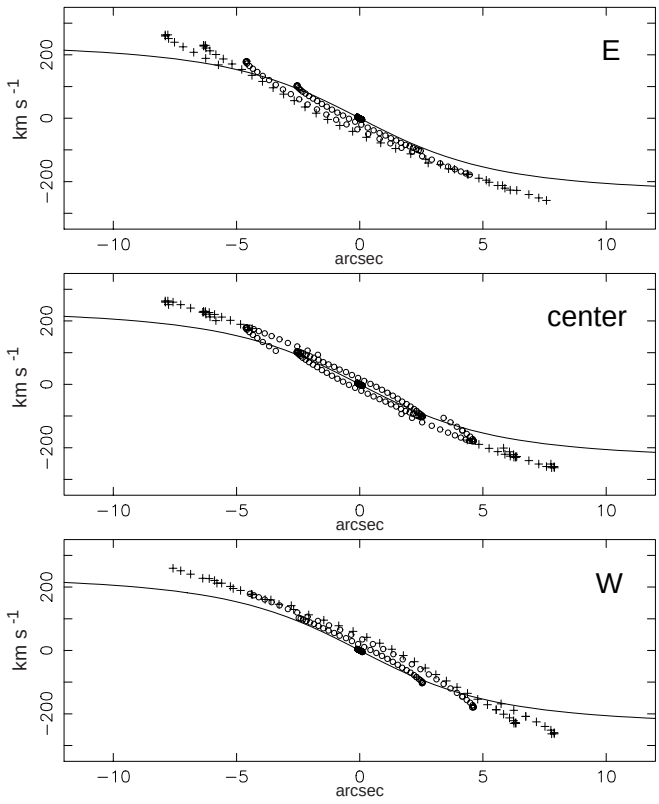

FIG. 14.—Model PV diagrams for the orbits within the outer ILR. The diagrams are cut along the major axis for east ($y > 0''$), center and west ($y < 0''$) sides, where y is the vertical axis on Fig. 12 (*top*). The cut has a $10''$ width in the galaxy's face-on plane. The symbols are the same as those in Fig. 12 (*bottom*): crosses are x_2-orbits, and circles are x_1-orbits inside the inner ILR. The model well represents the bends (*top and bottom panels*) and twist (*middle panel*) discussed in § 3.3 (see Fig. 10).

enhanced CO emission in the zeroth-moment map of NGC 3079 (Fig. 2) may arise from the high gas densities in the crowded regions. The streamlines belonging to the x_1-orbits extend entirely to the disk, producing the main disk.

Our model streamlines have sharp turns at the spiral arms. Such features, accompanied by shocks, have been observed by other authors (Athanassoula 1992; Athanassoula & Bureau 1999) in full hydrodynamical simulations. These turns can produce double-peaked features in line profiles observed along the spiral arms (Fig. 9) and agree spatially with the S-shaped twists on the first-moment map of NGC 3079 (Fig. 2). Figure 13 shows a comparison between the observed and model PV diagrams; contours are from the observed one, while the symbols show the model one, where different symbols are used for gaseous particles on the spiral arms (*squares*) and on the main disk (*dots*). On this diagram the main disk and spiral arms of NGC 3079 again agree well with the gaseous x_1-orbits and their crowding, respectively. This match between the observations and the model suggests that the main disk and spiral arms result from gaseous x_1-orbits and their associated crowding, respectively.

In the context of our model, gas streamlines on the downstream side of the sharp turns are nearly perpendicular to our line of sight. Thus the line-of-sight velocity of the gas indicates the pattern speed of the bar. We estimate the pattern speed from the gradient of the spiral arms on the observed PV diagram, which appears to be $\Omega_b = 55 \pm 10$ km s^{-1} kpc^{-1}; this is our adopted value to describe gas orbits, and it is consistent with the results of other authors (60 km s^{-1} kpc^{-1}; Veilleux et al. 1999, where the coincidence of corotation and the bar end was assumed).

4.3. *The Origin of The Nuclear Disk*

The nuclear disk may result from gaseous x_2-orbits. In Figure 13 the model PV diagram shows that the gaseous x_2-orbits (*crosses*) are in good agreement with the nuclear disk of NGC 3079. Figure 14 displays PV diagrams along the galaxy major axis for the orbits within the outer ILR. The three panels show PV cuts with $10''$ width (intrinsic to the galaxy) and positional offsets for the east, central, and west sides of the model galaxy, respectively. These panels reveal that the bends and twist of the ridges discussed in § 3.3 (see Fig. 10) are also reproduced in our model: the top and bottom panels show bends downward and upward, respectively, while the middle panel shows a twist upward (*left-hand side*) and downward (*right-hand side*). Since a purely rotating disk cannot produce this type of symmetric bends and twist, the gas on the nuclear disk must take oval orbits. Our gaseous x_2-orbits naturally reproduce the observed properties of the nuclear disk.

For later discussion in § 4.4, we mention the position angle of the x_2-orbits on the nuclear disk here in advance. The major axis of the orbits are inclined counterclockwise to the south from our line of sight in our current configuration (Fig. 11). On the other hand, orbits inclined in the opposite direction can also reproduce the nuclear disk on the PV diagram (Fig. 4). These orbits, however, make the ridges on the eastern and western PV diagrams (Fig. 14) bend in opposite directions and thus cannot match the

observations (Fig. 10). Therefore the orbits on the nuclear disk must have an inclination southward (counterclockwise) on the sky from our line of sight, like our gaseous x_2-orbits.

Many barred galaxies show an intense concentration of CO emission in their central parts (Sakamoto et al. 1999b, 2000). NGC 3079 also has such concentration in the nuclear disk region (see Fig. 8). This feature is well explained in the scenario of gas motions in bar: gas flow on x_1-orbits like ours leads to offset shocks at the leading edge of a bar and results in an inflow of gas toward the nuclear region. Then the inflowing gas on the x_1-orbits collides with gaseous x_2-orbits near the pericenter of the x_1-orbits, entering onto the gaseous x_2-orbits and thus increasing mass densities in the nuclear disk. This scenario has been confirmed in hydrodynamical simulations (Piner, Stone, & Teuben 1995; Athanassoula & Bureau 1999).

4.4. *The Origin of The Nuclear Core*

Our current model naturally explains the main features of the molecular disk of NGC 3079, which are the consequences of gas motions in a weak bar. However, the model does not explain the nuclear core, which appears in the PV diagram as high-velocity peaks near the galaxy center (Fig. 4). Owing to our ability to match the observations with our model for a bar, we attribute the high velocities to another origin, a massive central component, besides the bar. There still is a small possibility that the high velocities may arise from gaseous x_1-orbits within the inner ILR, which could elongate along our line of sight. However, the gaseous x_1-orbits are not the likely origin for two reasons.

1. Our gaseous x_1-orbits within the inner ILR (7.″7) look nearly circular and thus cannot show high velocities at their pericenter. Numerical experiments have also shown similar features: circular orbits in the innermost regions (Piner et al. 1995; Athanassoula & Bureau 1999). In the intensive study of PV diagrams for galaxies with bars by Bureau & Athanassoula (1999) and Athanassoula & Bureau (1999), the x_1-orbits within the inner ILR do not produce any remarkable features (and velocity peaks) on the PV diagrams. These all imply no significant contribution of the x_1-orbits within the inner ILR to our PV diagram.
2. Even if the gaseous x_1-orbits are elongated, they must be near perpendicular to our line of sight and cannot show us high velocities that occur at their pericenter, because the position angles ψ of x_1- and x_2-orbits, measured clockwise from the bar to the north (Fig. 12, *top panel*), are intrinsically $\psi_{x_1} = 0^\circ$ and $\psi_{x_2} = 90^\circ$, respectively, for collisionless stars. Owing to the damping force (working as viscosity), the two orbits drag each other and make $\psi_{x_1} > 0^\circ$ and $\psi_{x_2} < 90^\circ$ for collisional gas. This mechanism does not allow ψ_{x_1} to become larger than ψ_{x_2}. In addition to $\psi_{x_1} < \psi_{x_2}$, our gaseous x_2-orbits (nuclear disk) of NGC 3079 have to be inclined southward (counterclockwise) on the sky from our line of sight for the reason discussed in § 4.3. Thus the elongated gaseous x_1-orbits (if they exist) must be near perpendicular to our line of sight, and they cannot show the observed high-velocity features.

There are many disk galaxies that exhibit double bars, i.e., global and nuclear bars (e.g., Shaw et al. 1995; Friedli et al. 1996; Erwin & Sparke 1999). If NGC 3079 has a nuclear bar other than our global bar, it may result in the observed high-velocity features. This, however, is not the likely origin because such a nuclear bar is also thought to be a consequence of the x_1- and x_2-orbits in our global bar, whose orientations cannot be aligned with our line of sight. Recently, Heller, Shlosman, & Englmaier (2001) argued that a nuclear bar could be dynamically decoupled with a global bar in an evolutional phase, having a random orientation from the global bar. In that phase the x_1- and x_2-orbits have disappeared (Heller et al. 2001), which is not the case for NGC 3079.

Central components with high velocities are often found in rotation-curve studies of external galaxies (Sofue et al. 1999). They are attributed to central massive components (Sofue et al. 1999; Takamiya & Sofue 2000), while gas streaming motions in a bar could be another possible origin (Sakamoto et al. 1999a). In this section, we clarified detailed kinematics and the effect of a bar on the gas disk of NGC 3079 and argued that the high velocity should be attributed to a massive component at the galaxy center.

5. CENTRAL ROTATION CURVE AND MASSIVE CORE

We argued in § 4.4 that the high-velocity peaks at the radius of $\sim 1''$ in the PV diagram are not likely to result from noncircular motions driven by a bar but are a consequence of circular rotation around the nuclear core. We here estimate the central dynamical mass using a rotation curve.

5.1. *Central Rotation Curve*

The observed PV diagram in the galaxy center suffers from large intrinsic velocity dispersions and spill-in of emission from outer low-velocity components owing to the finite spatial resolution and slit width. Thus the central rotation curve is not straightforwardly obtained from an observed PV diagram. We adopt the Takamiya & Sofue (TS) method (T. Takamiya & Y. Sofue 1999, private communication; see Sofue & Rubin 2001) to obtain the rotation curve of the nuclear core. This method is designed to iteratively determine a rotation curve in an innermost region of a galaxy so that a model PV diagram calculated from the rotation curve and the galaxy's emission profile could reproduce the original diagram.

Figure 15 displays PV diagrams and rotation curves of the nuclear core: the left-hand panel shows the observed one along the galaxy major axis with $1''$ slit width, while the middle and right-hand panels show the calculated ones in the TS method and in the peak-tracing method, respectively. The emission profile at the center ($\sim 1''$) cannot be derived directly from our data owing to our spatial resolution ($\sim 2''$). But the observations are indicative of its very sharp gradient, because even a point source can reproduce our observed profile through a convolution with the synthesized beam. Thus we assumed the emission profile as an analytic function of an exponential with the scale length of $1''$, which well reproduces observed features on the PV diagram. We assumed intrinsic velocity dispersions of 60 km s^{-1} (e.g., 15–50 km s^{-1} in the Galactic center from Bally, Stark, & Wilson 1988, which is less active than NGC 3079).

The PV diagram and rotation curve from the TS method show that the envelope of the observed PV diagram requires a sharp rise of the rotation curve at the central region. The observed emission at around 0 km s^{-1}, which is not well reproduced in the TS method, may be contaminated by the

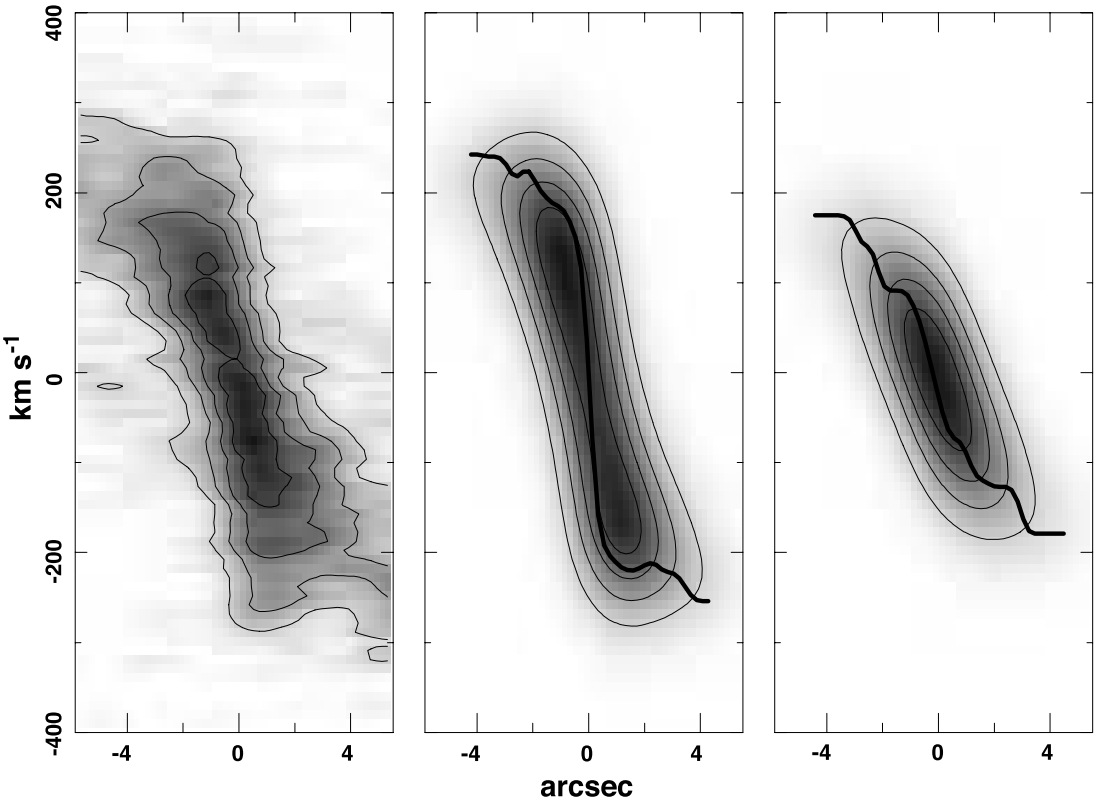

FIG. 15.—PV diagrams and rotation curves. The slit is 1″ wide. Contours are 20%, 40%, 60%, 80% of the peak intensity in each panel. *Left:* Observed PV diagram in the central region of NGC 3079. *Middle:* PV diagram and rotation curve derived in the Takamiya & Sofue method. *Right:* PV diagram and rotation curve derived in the peak-tracing method.

emission from the nuclear disk surrounding the nuclear core. For comparison, the right-hand panel displays the PV diagram using the rotation curve derived by tracing peak-intensity velocities of the observed PV diagram (the peak-tracing method); this method is often used to obtain rotation curves but fails to reproduce the observed high velocity at the central part.

5.2. *Mass Estimation and Central Massive Core*

The dynamical mass within a radius r is estimated by

$$M_{\rm dyn} = 2.3 \times 10^5 \left(\frac{r}{\rm kpc}\right)\left[\frac{v(r)}{\rm km\ s^{-1}}\right]^2 M_\odot\ . \qquad (4)$$

Our spatial resolution is about 2″ (152 pc), and the rotation velocity at this radius is 220 km s^{-1} from the rotation curve in the TS method (Fig. 15, *middle panel*). Thus the dynamical mass within the central 152 pc of NGC 3079 is estimated to be $M_{\rm dyn} = 1.7 \times 10^9\ M_\odot$. The ratio of dynamical mass to the total molecular gas mass ($3.0 \times 10^8\ M_\odot$ from § 3.4) in the nuclear core is $M_{\rm gas}/M_{\rm dyn} = 18\%$.

The rotation curve is meaningful at the radius less than 2″, even though the spatial resolution is only ∼2″: We can distinguish two emission peaks only if their spatial separation is larger than 2″ on a single-channel map or zeroth-moment map. However, on the PV diagram and rotation curve, the additional parameter, velocity, provides a finer spatial resolution, because two emission peaks with different velocities can be resolved in the PV diagram even if their separation is less than 2″. Then the spatial resolution will be determined by the typical error of a Gaussian fit to a point source, which depends on the signal-to-noise ratio, and in our case is $\ll$1″ (see Condon 1997). Therefore the velocity of 200 km s^{-1} at the radius of 1″ (76 pc) is meaningful, and it implies a dynamical mass of $M_{\rm dyn} = 7.0 \times 10^8\ M_\odot$ within the radius of 76 pc. The derived masses are listed in Table 4.

Recently, central supermassive black holes with mass 10^7–$10^8\ M_\odot$ have been found in many AGNs (Miyoshi et al. 1995; Wandel et al. 1999; Ishihara et al. 2001). In the case of NGC 3079, VLBI observations of H_2O maser emission indicate that its central mass within 0.5 pc is $\sim 10^6\ M_\odot$ (Trotter et al. 1998). Thus our mass $\sim 10^9\ M_\odot$ within ∼100 pc cannot be attributed to this central supermassive black hole. The connection between this large dynamical mass and the nuclear outflow in parsec scale (Henkel et al. 1984; Irwin & Seaquist 1988; Trotter et al. 1998) and kiloparsec scale (Duric & Seaquist 1988; Ford et al. 1986) in this galaxy will be an interesting issue for future investigations.

6. CONCLUSIONS

We have made CO (1–0) observations of the Hα/radio lobe galaxy NGC 3079 with the Nobeyama Millimeter Array and reported characteristic features and gas dynamics in the molecular disk in the central 4.5 kpc (1′).

1. Our observations show four distinct components in the molecular disk: the main disk, spiral arms, nuclear disk, and nuclear core.

2. The main disk extends along the galaxy major axis. We detected the inner region of this component, within the

radius of ~2 kpc on a zeroth-moment map, while its full extent is not covered in our synthesis observations. Molecular gas shows a smooth distribution on the main disk and has a gas mass of $5 \times 10^9\ M_\odot$ within the central ~2 kpc.

3. The spiral arms are superimposed on the main disk, forming an inverted S-shaped pattern on the sky. Abrupt velocity changes of up to ~200 km s^{-1} are observed along the spiral arms, in S-shaped twists of isovelocity contours and in double velocity-peaked features on the spectra. This component and the nuclear disk form a figure-of-eight pattern on a PV diagram, which sometimes appears in edge-on barred galaxies.

4. The nuclear disk, appearing in PV diagrams, has an extent of ~600 pc radius. The molecular gas is intensely concentrated on the nuclear disk, where the gas surface density is an order of magnitude higher than that typical of nearby galaxies. Its appearance (bends and twist) on PV diagrams is indicative of oval rather than circular motions in the gas. And the position angle of the oval orbits is inclined southward from our line of sight.

5. The nuclear core has a radius smaller than ~150 pc, which is unresolved in our current observations. The gas mass within the central ~150 pc amounts to $3 \times 10^8\ M_\odot$. This component shows a very high velocity ~200 km s^{-1} at the radius of the central ~100 pc on the PV diagram.

6. A weak bar model explain the features of the main disk, spiral arms, and nuclear disk in zeroth- and first-moment maps, PV diagrams, and the spectrum at each spatial point. The main disk and spiral arms result from gaseous x_1-orbits and their crowding, respectively. The nuclear disk arises from gaseous x_2-orbits. The gas concentration in the nuclear disk is also explained in the context of our model: the gas on x_1-orbits moves along spiral arms (or offset shocks), collides with the gas on x_2-orbits, and is accumulated onto the nuclear disk. Assuming that the gas in spiral arms moves along streamlines perpendicular to our line of sight, the pattern speed of the bar can be estimated to be 55 ± 10 km s^{-1} kpc^{-1}.

7. Our model for a bar, however, does not explain the high velocity of the nuclear core. Moreover, any orbit caused by a bar is not likely to produce that component. Thus we attribute it to a central massive core with a dynamical mass of $10^9\ M_\odot$ within the central 100 pc, which is 3 orders of magnitude more massive than the mass of a central supermassive black hole.

We are grateful to the NRO staff and Rainbow team members for their help with observations. We thank Toshihito Shibatsuka for kindly showing his results prior to publication. We also thank the referee for useful comments. J. K. thanks Toshihiro Handa for careful reading of the manuscript and fruitful comments, Keiichi Wada for useful discussions and continuous encouragements, and Kentaro Aoki for his help with the analysis of the *HST* data. J. K. was financially supported by the Japan Society for the Promotion of Science for Young Scientists.

REFERENCES

Achtermann, J. M., & Lacy, J. H. 1995, ApJ, 439, 163
Arimoto, N., Sofue, Y., & Tsujimoto, T. 1996, PASJ, 48, 275
Athanassoula, E. 1992, MNRAS, 259, 345
Athanassoula, E., & Bureau, M. 1999, ApJ, 522, 699
Bally, J., Stark, A. A., & Wilson, R. W. 1988, ApJ, 324, 223
Binney, J. Gerhard, O. E., Stark, A. A., Bally, J., & Uchida, K. I. 1991, MNRAS, 252, 210
Brandt, J. C. 1965, MNRAS, 129, 309
Braine, J., et al. 1993, A&AS, 97, 887
Bureau, M., & Athanassoula, E. 1999, ApJ, 522, 686
Cecil, G., Bland-Hawthorn, J., Veilleux, S., & Filippeko, A. V. 2001, ApJ, 555, 338
Clemens, D. P., Sanders, D. B., & Scoville, N. Z. 1988, ApJ, 327, 139
Combes, F., Debbasch, F., Friedli, D., & Pfenniger, D. 1990, A&A, 233, 82
Condon, J. J. 1997, PASP, 109, 166
Cox, A. N. 2000, Allen's Astrophysical Quantities (4th ed; New York: Springer)
Dame, T. M., Hartmann, D., & Thaddeus, P. 2001, ApJ, 547, 792
de Vaucouleurs, G., de Vaucouleurs, A., Corwin, H. G., Buta, R. J., Paturel, G., & Fouqué, P. 1991, Third Reference Catalog of Bright Galaxies (New York: Springer)
Duric, N., & Seaquist, E. R. 1988, ApJ, 326, 574
Erwin, P., & Sparke, L. S. 1999, ApJ, 521, L37
Fabbiano, G., Kim, D.-W., & Trinchieri, G. 1992, ApJS, 80, 531
Filippenko, A. V., & Sargent, W. L. W. 1992, AJ, 103, 28
Ford, H. C., Dahari, O., Jacoby, G. H., Crane, P. C., & Ciardullo, R. 1986, ApJ, 311, L7
Friedli, D., Wozniak, H., Rieke, M., Martinet, L., & Bratschi, P. 1996, A&AS, 118, 461
García-Burillo, S., & Guélin, M. 1995, A&A, 299, 657
Handa, T., Nakai, N, Sofue, Y., Hayashi, M., & Fujimoto, M. 1990, PASJ, 42, 1
Handa, T., Sofue, Y., Ikeuchi, S., Kawabe, R., & Ishizuki, S. 1992, PASJ, 44, L227
Hawarden, T. G., Israel, F. P., Geballe, T. R., & Wade, R. 1995, MNRAS, 276, 1197
Heckman, T. M. 1980, A&A, 87, 152
Heckman, T. M., Armus, L., & Miley, G. K. 1990, ApJS, 74, 833
Heller, C., Shlosman, I., & Englmaier, P. 2001, ApJ, 553, 661
Henkel, C, Güsten, R., Downes, D., Thum, C., Wilson, T. L., & Biermann, P. 1984, A&A, 141, L1
Ho, L. C., Fillipenko, A. V., & Sargent, W. L. W. 1997, ApJS, 112, 315
Irwin, J. A., & Seaquist, E. R. 1988, ApJ, 335, 658
———. 1991, ApJ, 371, 111
Irwin, J. A., & Sofue, Y. 1992, ApJ, 396, L75
Ishihara, Y., Nakai, N., Iyamoto, N., Makishima, K., Diamond, P., & Peter, H. 2001, PASJ, 53, 215
Koda, J., & Wada, K. 2002, ApJ, submitted
Kohno, K., et al. 2001, in ASP Conf. Ser. 249, The Central kpc of Starbursts and AGNs, ed. J. H. Knapen, J. E. Beckman, I. Shlosman, I., & T. J. Mahoney (San Francisco: ASP), 672
Kuijken, K., & Merrifield, M. R. 1995, ApJ, 443, L13
Laine, S., Kenney, J. D. P., Yun, M. S., & Gottesman, S. T. 1999, ApJ, 511, 709
Lindblad, P. O., & Lindblad, P. A. B. 1994, in ASP Conf. Ser. 66, Physics of the Gaseous and Stellar Disks of the Galaxy, ed. I. R, King (San Francisco: ASP), 29
Merrifield, M. R., & Kuijken, K. 1999, A&A, 345, L47
Miyoshi, M., Moran, J., Henstein, J., Greenhill, L., Nakai, N., Diamond, P., & Inoue, M. 1995, Nature, 373, 127
Nakai, N., Inoue, M., Miyazawa, K., Miyoshi, M., & Hall, P. 1995, PASJ, 47, 771
Okumura, S. K., et al. 2000, PASJ, 52, 393
Pérez García, A. M., Rodríguez Espinosa, J. M., & Fuensalida, J. J. 2000, ApJ, 529, 875
Pietsch, W. Trinchieri, G., & Vogler, A. 1998, A&A, 340, 351
Piner, B. G., Stone, J. M., & Teuben, P. J. 1995, ApJ, 449, 508
Regan, M. W., Thornley, M. D., Helfer, T. T., Sheth, K., Wong, T., Vogel, S. N., & Bock, D. C.-J. 2001, ApJ, 561, 218
Sakamoto, K., Baker, A. J., & Scoville, N. Z. 2000, ApJ, 533, 149
Sakamoto, K., Okumura, S. K., Ishizuki, S., & Scoville, N. Z. 1999a, ApJS, 124, 403
———. 1999b, ApJ, 525, 691
Sandage, A., & Tamman, G. 1981, A Revised Sharpley-Ames Catalog of Bright Galaxies (Washington, DC: Carnegie Institution of Washington)
Sawada-Satoh, S., Inoue, M, Shibata, K. M., Kameno, S., & Migenes, V. 2000, PASJ, 52, 421
Shaw, M. A., Axon, D. J., Probst, R., & Gatley, I. 1995, MNRAS, 274, 369
Shaw, M., Wilkinson, A., & Carter, D. 1993, A&A, 268, 511
Sofue, Y., & Irwin, J. A. 1992, PASJ, 44, 353
Sofue, Y., Koda, J., Kohno, K., Okumura, S. K., Honma, M., Kawamura, A., & Irwin, J. A. 2001, ApJ, 547, L115
Sofue, Y., & Rubin, V. 2001, ARA&A, 39, 137
Sofue, Y., Tutui, Y., Honma, M., Tomita, A., Takamiya, T., Koda, J., & Takeda, Y. 1999, ApJ, 523, 136
Soifer, B. T., Boehmer, L., Neugebauer, G., & Sanders, D. B. 1989, AJ, 98, 766
Sosa-Brito, R. M., Tacconi-Garman, L. E., & Lehnert, M. D. 2001, ApJS, 136, 61
Takamiya, T., & Sofue, Y. 2000, ApJ, 534, 670

Trotter, A. S., Greenhill, L. J., Moran, J. M., Reid, M. J., Irwin, J. A., & Lo, K. Y. 1998, ApJ, 495, 740
Veilleux, S., Bland-Hawthorn, J., & Cecil, G. 1999, AJ, 118, 2108
Veilleux, S., Cecil, G., Bland-Hawthorn, J., & Tully, R. B. 1994, ApJ, 433, 48
Wada, K. 1994, PASJ, 46, 165
Wada, K., & Koda, J. 2001, PASJ, 53, 1163
Wandel, A., Peterson, B. M., & Malkan, M. A. 1999, ApJ, 526, 579
Young, J. S., Claussen, M. J., & Scoville, N. Z. 1988, ApJ, 324, 115
Young, J. S., et al. 1995, ApJS, 98, 219
Zacharias, N., et al. 2000, AJ, 120, 2131